First-principles studies of the metal atom dependent physical properties of one-dimensional metal-cluster nanowires $X_4OTe_9I_4$ (X = Nb, Ti)

Fumin Zhang and Huabing Yin [*]

Institute for Computational Materials Science, Joint Center for Theoretical Physics, and International Joint Research Laboratory of New Energy Materials and Devices of Henan Province, School of Physics and Electronics, Henan University, Kaifeng 475004, China

Metal-cluster compounds have recently attracted attention in the quest for novel low-dimensional multifunctional semiconductors owing to the structural diversity of metal-cluster geometries and the resulting broken symmetries. Based on first-principles calculations, we proposed a one-dimensional (1D) metal-cluster family of $X_4OTe_9I_4$ (X = Nb, Ti) nanowires with high stability. Due to differences in the number of valence electrons of the metal atoms (Nb and Ti), these two nanowires exhibit distinct chain structures and physical properties. Our calculations revealed that $Nb_4OTe_9I_4$ and $Ti_4OTe_9I_4$ nanowires were direct- and indirect-band-gap semiconductors with moderate gaps of 1.32 and 1.25 eV, respectively. The off-center displacement of Nb ions in the optimized $Nb_4OTe_9I_4$ nanowire induced intrinsic chain-direction ferroelectric ordering, whereas the $Ti_4OTe_9I_4$ nanowire with a similar chain structure maintained a stable nonferroelectric structure. The structural evolution of the two nanowires under the tensile strain displayed different behaviors. When the tensile strain was applied, the $Nb_4OTe_9I_4$ nanowire tended to shrink toward the cluster structure to stabilize the polar structure and produce the unexpected force release, whereas $Ti_4OTe_9I_4$ nanowire was uniformly stretched before fracture. In addition, tunable magnetism was introduced into these two nonmagnetic 1D systems using carrier doping and alloying methods. On the one hand, the alloying process regulated the band gap of the material; on the other hand, it altered the spin-electronic properties of the system. Our calculations indicate that $X_4OTe_9I_4$ (X = Nb, Ti) nanowires serve as representative 1D multifunctional materials, which are crucial for studying the structure-determined properties of low-dimensional materials.

I. INTRODUCTION

Originating with graphene and extending to various layered van der Waals (vdW) materials, the successful isolation of individual atomic layers from their bulk crystals through exfoliation methods has garnered growing interest in the field of two-dimensional (2D) materials [1,2]. The exploration has unveiled new fundamental physics and highlighted potential applications across a wide spectrum of fields [3–7]. In contrast with 2D layered materials, atomically thin one-dimensional (1D) vdW materials exhibit unique physical and chemical properties owing to the quantum confinement of electrons and phonons along a single dimension [8–10]. Therefore, 1D vdW materials have garnered widespread interest and have been harnessed for various applications, including optics, electronics, catalysts, and nanomechanics. In addition to vapor- and solution-phase growth [11,12], electrodeposition [13,14], and encapsulation in templates [15,16], physical exfoliation is an effective technique for fabricating 1D vdW materials [17–19]. With the rapid advancement of exfoliation techniques, numerous vdW-stacked materials have been successfully converted into 1D chains or nanowires using exfoliation methods, such as micromechanical or solution processes. Examples include but are not limited to experimentally synthesized 1D Te

[17], Nb_2Se_9 [18], and $CrSbSe_3$ [19]. Theoretical simulation methods play a crucial role in predicting the structures and properties of 1D materials [20–22].

Ferroelectric materials exhibit charge dipole formation, causing spontaneous orders that generate macroscopic polarizations. These polarizations can be altered by applying an external fields. Consequently, researchers have directed significant attention toward ferroelectric materials owing to their substantial technical merits for various applications, including nonvolatile memories, sensors, ferroelectric tunnel junctions, and photovoltaics [23–25]. The exploration of novel semiconductor devices based on 1D nanostructures represents a burgeoning direction in the field of low-dimensional materials; a series of 1D and quasi-1D inorganic ferroelectric candidates have been experimentally and theoretically identified. These include perovskite nanotubes [26,27], XN (X = Bi, Sb) [28], WOX_4 (X = F, Cl, and Br) [29], and MS (M = Ge, Sn) [30,31]. Building on the experimental observations on SnTe nanowires, various 1D nanostructures have been successfully fabricated within carbon nanotubes (CNTs) [4,32,33]. Furthermore, ferroelectricity has been demonstrated in 1D organic polymer structures. With the successful experimental fabrication of actinide endohedral fullerenes, Zhang *et al.* designed a series of 1D fullerene-based chains, namely, $U_2C@C_{80}$-M (M = Cr, Mn, Mo, and Ru), which exhibited both ferroelectric and ferromagnetic properties [34]. Currently, researchers are motivated to explore novel 1D

*yhb@henu.edu.cn

materials, both theoretically and experimentally, along this promising route.

Considering their structural diversity and chemical or physical properties, the unique combination of metal, chalcogen, and halogen elements constitutes an intriguing class of species. Upon the addition of oxygen, a series of O-centered tetranuclear fragments called transition metal halides (TM-CHs) are formed. Within these tetranuclear fragments, the complexes exhibit either a square or distorted tetrahedral arrangement of metal atoms surrounding the central chalcogen atom, and the metal atoms are interconnected by chalcogenide and halogenide bridging ligands. The highly sophisticated coordination chemistry of TMCHs has led to the discovery of various compounds with diverse properties. Notably, tetranuclear complexes, such as $X_4OTe_9I_4$ (X = Ta, Nb, Ti) [35–37], $V_4OSe_8I_8$ [38], $Ti_4OX_8Br_6$ (X = S, Se) [39], $Ti_4OS_8Cl_6$ [40], $Ta_4S_9Br_8$ [41], $Ta_4Se_9I_8$ [42], and $V_4S_9Br_4$ [43], have gained recognition. Numerous cluster complexes with varied functionalities have been derived from TMCHs compounds containing heavy group IV, V, and VI transition metals [44–46].

Some TMCHs materials, such as bulk $Nb_4OTe_9I_4$ [36] and $Ti_4OTe_9I_4$ [37], exhibit typical quasi-1D chain-stacking structures. Therefore, the 1D structures of $Nb_4OTe_9I_4$ and $Ti_4OTe_9I_4$ are expected to be synthesized experimentally. These two structures share common characteristics characterized by clusters of four metal atoms, which hold special significance in materials chemistry. Generally, for tetranuclear cluster complexes, the electron concentration in group VI compounds is sufficiently high to support metal-metal cluster bonding; however, some clusters formed by electron-poor transition metals in groups III and IV require the encapsulation of interstitial atoms to stabilize the structure [36,47]. The clusters of group V elements represent borderline cases. The interstitial atom acts as an electron donor to stabilize metal-metal bonds and forms strong metal-interstitial bonds to stabilize the cluster [40]. In $Nb_4OTe_9I_4$ and $Ti_4OTe_9I_4$ crystals, the interstitial atoms are O atoms. Owing to their differing electron-poor features, Nb and Ti atoms exhibit distinct chemical bonds with interstitial O atoms, resulting in significant differences in the structure and properties of 1D $Nb_4OTe_9I_4$ and $Ti_4OTe_9I_4$ nanowires, particularly in electronic, ferroelectric, and mechanical properties. Understanding the variations in physical properties that arise from similar structures and different coordination environments is crucial for material design.

In this study, using first-principles calculations, we predicted two 1D TMCHs nanowires, $Ti_4OTe_9I_4$ and $Nb_4OTe_9I_4$, characterized by O-centered tetranuclear fragments. They were prepared from bulk crystals using exfoliation methods. The polar $Nb_4OTe_9I_4$ nanowire exhibited ferroelectric distortions with a large spontaneous polarization. Conversely, the $Ti_4OTe_9I_4$ nanowire exhibited a nonpolar structure in the axial direction. Ferroelectric polarization can modulate the electronic and mechanical properties of nanowires. The two nanowires exhibited different structure evolution behaviors under strain. In particular, $Nb_4OTe_9I_4$ nanowire experienced an unexpected force-releasing stage when the external strain was increased to 11% and tended to form clusters to stabilize the polar structure. However, the nonferroelectric $Ti_4OTe_9I_4$

nanowire was always linearly stretched. Furthermore, magnetism was introduced into the nanowire systems through carrier doping and alloying. By alloying Nb and Ti in 1D $X_4OTe_9I_4$ nanowires, we obtained several promising magnetic semiconductors with large band gaps. Our calculations indicate that the $X_4OTe_9I_4$ (X = Nb, Ti) nanowires may have potential applications in flexible electronic and spintronic devices.

II. COMPUTATIONAL METHODS

The first-principles calculations were performed by using density functional theory (DFT) within the Vienna *ab initio* simulation package (VASP) [48,49]. The Perdew-Burke-Ernzerhof generalized gradient approximation (GGA-PBE) was employed as the exchange-correlation functional [50]. The vdW interactions were accounted for by incorporating DFT-D3 corrections [51]. Following convergence tests, a plane-wave basis with a kinetic energy cutoff of 600 eV was utilized to describe electron wave functions. The first Brillouin zone was sampled using the Γ-centered Monkhorst-Pack scheme with a grid of $1 \times 1 \times 10$ k points. To prevent interaction between adjacent nanowires under periodic boundary conditions, a vacuum region larger than 20 Å was implemented. Convergence criteria for energy between two ionic steps and force on each atom were set to be less than 10^{-6} eV and 0.01 eV/Å, respectively. The Heyd-Scuseria-Ernzerhof (HSE06) hybrid functional was employed to enhance the accuracy of electronic calculations [52]. Phonon dispersion was determined in a $1 \times 1 \times 4$ supercell using the finite displacement method in the PHONOPY package [53]. The evaluation of spontaneous electric polarization was conducted through modern polarization theory based on the Berry phase approximation [54,55]. The minimum-energy pathways for ferroelectric transitions were determined using the climbing image nudged elastic band (CI-NEB) method [56,57]. The electrical transport parameters were calculated using the Boltzmann transport theory, as implemented in the BOLTZTRAP2 code [58].

III. RESULTS AND DISCUSSION

A. Crystal structure

In the early 1990s, several TMCH compounds with relatively loose interchain contacts were successfully synthesized and structurally characterized, including $Nb_4OTe_9I_4$ and $Ti_4OTe_9I_4$ with the space group $C2/c$ (No. 15) [36,37]. In each unit cell, both the bulk $Nb_4OTe_9I_4$ and $Ti_4OTe_9I_4$ crystals consisted of four nanowires running alternately and parallel to the crystallographic z axis and held together solely by vdW contacts [see Figs. 1(a) and 1(b)]. The lattice parameters and angles computed using the PBE method are summarized in Table I and show excellent agreement with the experimental results.

The vdW interaction characteristic indicates the potential for exfoliating the 1D $Nb_4OTe_9I_4$ and $Ti_4OTe_9I_4$ nanowires from their bulk crystals. The calculated exfoliation energies of $Nb_4OTe_9I_4$ and $Ti_4OTe_9I_4$ nanowires are 101 and 106 meV/atom, respectively, which are comparable to that of 2D MoS_2 ($\approx$77 meV/atom) [59], and lower than those of

TABLE I. The space group, lattice parameters (a, b, and c in Å), angle (β in °), average bond lengths ($\bar{l}_{Nb(Ti)-Nb(Ti)}$, $\bar{l}_{Nb(Ti)-Te}$, and $\bar{l}_{Nb(Ti)-O}$), and axial offset of O atom relative to the Nb planes ($|\Delta d|$) for the 1D and bulk $X_4OTe_9I_4$ (X = Nb, Ti) systems in theory and experiment.

System	Space group	a (Å)	b (Å)	c (Å)	$\beta(°)$	$\bar{l}_{Nb(Ti)-Nb(Ti)}$ (Å)	$\bar{l}_{Nb(Ti)-Te}$ (Å)	$\bar{l}_{Nb(Ti)-O}$ (Å)	$|\Delta d|$ (Å)
1D $Nb_4OTe_9I_4$	$P2$			6.22		3.07, 3.67, 3.90	2.80	2.16, 1.98	0.39
Bulk $Nb_4OTe_9I_4$	$C2/c$	22.29	20.03	6.21	122.74	3.07, 3.65, 3.89	2.80	2.15, 1.98	0.39
Bulk $Nb_4OTe_9I_4$ (expt. [36])	$C2/c$	21.97	19.93	6.20	122.43	3.06, 2.68, 2.94	2.81	2.18, 2.00	0.40
1D $Ti_4OTe_9I_4$	$P\bar{4}$			6.28		3.17, 3.77, 3.77	2.80	2.07, 2.07	<0.01
Bulk $Ti_4OTe_9I_4$	$C2/c$	22.36	19.31	6.26	123.67	3.16, 3.73, 3.79	2.78	2.05, 2.07	<0.01
Bulk $Ti_4OTe_9I_4$ (expt. [37])	$C2/c$	22.14	19.13	6.23	125.51	3.17, 3.75, 3.79	2.78	2.05, 2.07	<0.01

already experimentally exfoliated 1D Se ($\approx$225 meV/atom) [60] and Te monatomic chains ($\approx$273 meV/atom) [17]. This confirms the high feasibility of exfoliating these 1D nanowires. The optimized lattice constants of $Nb_4OTe_9I_4$ and $Ti_4OTe_9I_4$ nanowires are $c = 6.22$ and 6.28 Å respectively, which are close to those of their bulk crystals. The corresponding structural parameters are summarized in Table I for comparison. Using $Nb_4OTe_9I_4$ as an example, the noncentrosymmetric chain structure of $Nb_4OTe_9I_4$ is shown in the top and side panels in Fig. 1(c). 1D $Nb_4OTe_9I_4$ belongs to $P2$ space group, wherein each chain comprises the distorted tetrahedral oxygen-centered clusters of Nb atoms with terminal I atoms and Te-bridged edges. The individual clusters are linked by Te atoms in the axial direction. In detail, at the cluster core, the chain compound $Nb_4OTe_9I_4$ shares a common Nb_4O framework that effectively stabilizes clusters. The Nb_4O core assumes the form of a flattened tetrahedron, with an interstitial O atom situated at its center. Each pair of adjacent Nb_4O cores connects isolated Te atoms, forming a chain along the z axis. In addition, each of the four pairs of Te_2 groups with the bond length $\bar{l}_{Te-Te} = 2.74$ Å forms bonds with an almost equally short Nb-Nb edge ($\bar{l}_{Nb-Nb} = 3.07$ Å),

and the Te-Te bond crosses over the short Nb-Nb edge. Concurrently, the two longer Nb-Nb edges are bridged by isolated Te atoms and central O atoms, exhibiting distinct distances, such as $\bar{l}_{Nb-Nb} = 3.67$ and 3.90 Å. In this system, all Nb-Te bonds are almost identical, with the length $\bar{l}_{Nb-Te} = 2.80$ Å. Furthermore, the variation in the bond length between Nb and O ($\bar{l}_{Nb-O} = 2.16$ and 1.98 Å) considerably impacts the vertical distance of O relative to the Nb planes on both sides, resulting in an axial offset ($|\Delta d| = |d_1 - d_2|/2$) of 0.39 Å for the 1D $Nb_4OTe_9I_4$ nanowire. This offset may lead to polarization in the axial direction.

When all the principal elements of Nb are substituted with Ti, the chain structure transforms into a nonpolar configuration in the chain direction. The $Ti_4OTe_9I_4$ nanowire belong to the $P\bar{4}$ space group and conform to the Ti_4O cluster core. Notably, the large distances between two diagonal Ti atoms are nearly equal, both measuring approximately 3.77 Å, whereas the length of the short Nb-Nb edge is 3.17 Å. For the $Ti_4OTe_9I_4$ nanowire, the O atom displaces along the z axis relative to the Ti planes on both sides, and the Ti-O bond length becomes uniform ($\bar{l}_{Ti-O} = 2.07$ Å). This small axial offset ($|\Delta d| < 0.01$ Å) results in a nonpolar structure in the axial direction. The distinct chain structures arising from the identical coordination environments may be attributed to the different outer electron configurations of the Nb and Ti atoms. The Nb atom retains one electron for bonding with the neighboring metal atoms, whereas the Ti atom does not. In addition, to examine the structural stability of the 1D $Nb_4OTe_9I_4$ and $Ti_4OTe_9I_4$ nanowires, their phonon dispersion spectra were calculated [Figs. 1(e) and 1(f), respectively]. The absence of an appreciable imaginary phonon mode in the phonon dispersions confirms their dynamical stability.
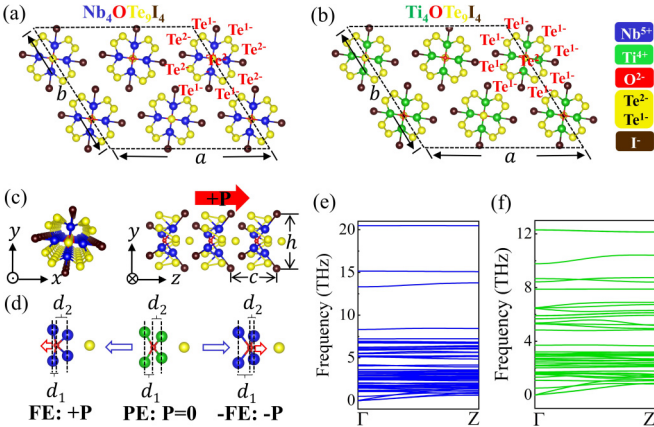
B. Ferroelectric polarization and switching barrier

In the 1D $Nb_4OTe_9I_4$ nanowire, the O ion in the axial direction exhibit an off-center displacement with respect to the Nb planes on both sides, resulting in a polarized structure. Under the influence of an external electric field, the polarization direction can reverse, exhibiting ferroelectricity. Similar ferroelectricity was predicted for $Ta_4OTe_9I_4$ nanowire with the same chain structure in our previous study [22]. However, the off-center displacement of the O atom in the $Ti_4OTe_9I_4$ nanowire is almost negligible. Thus, the 1D $Ti_4OTe_9I_4$ nanowire do not exhibit axial-direction polarization and ferroelectricity. The lattice distortion is defined in terms of the horizontal distance of the O atom from the Nb planes on both sides, denoted as d_1 and d_2, as shown in
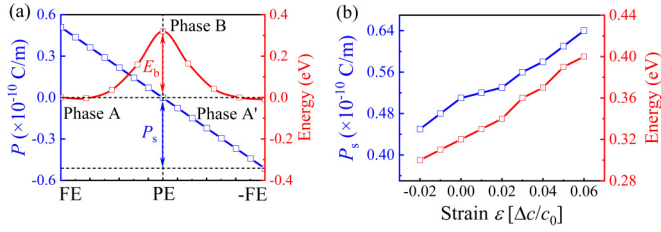

FIG. 1. Top views of the structures of bulk (a) $Nb_4OTe_9I_4$ and (b) $Ti_4OTe_9I_4$ materials. The blue, green, red, yellow and brown balls represent Nb, Ti, O, Te, and I atoms, respectively. (c) Top and side views of 1D $Nb_4OTe_9I_4$ nanowire. The lattice constant and lateral width of nanowires are labeled as c and h, respectively. (d) Side views of two energy degenerate distorted ferroelectric structures and undistorted paraelectric structure. The horizontal distance of chain-center red O atom respect to the Nb planes on both sides are labeled as d_1 and d_2. Phonon spectra of 1D (e) $Nb_4OTe_9I_4$ and (f) $Ti_4OTe_9I_4$ nanowires.

FIG. 2. (a) The energy and polarization of 1D $Nb_4OTe_9I_4$ nanowire in the ferroelectric transition process by using the CI-NEB method. P_s is spontaneous polarization and E_b represents the energy barrier of polarization switching. (b) The spontaneous polarization P_s and transition barrier E_b as a function of the strain ε.

Fig. 1(d). Two stable energy-degenerate ferroelectric configurations with opposites polarizations, FE and −FE states, are associated with one paraelectric state. The two ferroelectric states correspond to cases where $d_1 < d_2$ (FE) and $d_1 > d_2$ (−FE), respectively, whereas the paraelectric state is characterized by $d_1 = d_2$ (PE). The paraelectric phase of $Nb_4OTe_9I_4$ nanowire share the same space-group symmetry of $P\bar{4}$ with the $Ti_4OTe_9I_4$ nanowire. Nonpolar $Ti_4OTe_9I_4$ nanowire can stabilize this paraelectric structure.

The intrinsic ion-displacement ferroelectricity of $Nb_4OTe_9I_4$ nanowire arises from the cooperative displacement of O atom with respect to the Nb planes on both sides along the z direction. The spontaneous polarization aligned along the polarization axis is denoted as a scalar P_s, and P_s is calculated using the Berry phase within the modern theory of polarization. For 1D nanowires, an effective cross-sectional area is considered to estimate the P_s value. As shown in Fig. 1(c), the cross-sectional area is defined as $S = c \times h$, where c and h are the lattice constant and lateral width of $Nb_4OTe_9I_4$ nanowire, respectively. This is currently the common method for dealing with polarization in 1D materials [55,61], and it is conducive to comparing polarization with 2D materials. The P_s value is estimated to be 0.51×10^{-10} C/m, which is comparable to that of analogous $Ta_4OTe_9I_4$ nanowire [22]. In practical terms, the reversal of polarization can be achieved through a phase transition induced by an external electric field. As shown in Fig. 2(a), the ferroelectric switching proceeds through a direct transition involving the paraelectric configuration, and the transition barrier E_b determined using the CI-NEB method is 320 meV/f.u. [56], which is larger than that of conventional ferroelectric $PbTiO_3$ ($E_b \approx 219$ meV/f.u.) [62]. This implies that a relatively higher electric field is required for the reversal of polarization in $Nb_4OTe_9I_4$ nanowire compared with that in $PbTiO_3$. However, the estimated barrier energy is also comparable to or even lower than those of some other reported 1D, 2D, and bulk ferroelectrics, such as bulk-$BiFeO_3$ (430 meV/f.u.) [62], 2D Sc_2CO_2 (520 meV/f.u.) [63], 2D Hf_2CF_2 (423 meV/f.u.) [64], 1D SbN (486 meV/f.u.) [28], and 1D WOF_4 (523 meV/f.u.) [29]. In real situations, the process of reversing electric polarization is mediated by domain growth and domain-wall (DW) migration. The DW migration can generally lower the energy barrier of the $Nb_4OTe_9I_4$ nanowire. While this increases the possibility of experimentally achieving polarization reversal through an external electric field, significant challenges remain.
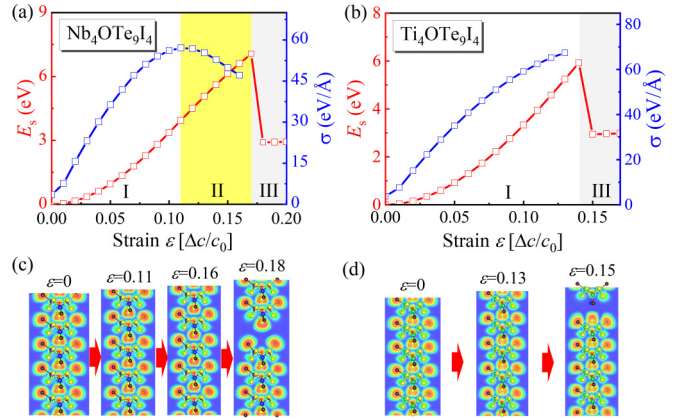

FIG. 3. The strain energy E_s (red) and tensile force σ (blue) as a function of the tensile strain ε in the (a) $Nb_4OTe_9I_4$ and (b) $Ti_4OTe_9I_4$ supercells. Ball-and-stick representations and 2D contour plots of the electronic charge density of the different stages along the stretching process of the (c) $Nb_4OTe_9I_4$ and (d) $Ti_4OTe_9I_4$ nanowires.

Notably, the bonding between the Nb and O ions remains intact during ferroelectric switching, although the bonding angle undergoes a dramatic change. An appropriate tensile strain along the chain direction increases the displacement of O atom with respect to the Nb planes on both sides, effectively enhancing the P_s and E_b values of the $Nb_4OTe_9I_4$ nanowire, as shown in Fig. 2(b). Conversely, the compressive strain decreases the P_s and E_b values. The promising ferroelectricity of $Nb_4OTe_9I_4$ nanowire effectively expands the family of 1D ferroelectric materials, playing a catalytic role in the application of ferroelectric materials.

C. Strain-related structure evolution

A particular concern regarding 1D structures is the fracture dynamics of the systems, which yield valuable information regarding structural changes, stiffness, and other mechanical features. To investigate these aspects, we constructed $1 \times 1 \times 5$ supercells ($X_4OTe_9I_4$, where $X =$ Nb or Ti) and subjected them to stretching along the periodic direction to analyze the structural evolution up to the breaking point. The variations in strain energy (E_s) versus strain (ε), $E_s = E(\varepsilon) - E(0)$, were calculated by incrementally enhancing the constant lattice uniformly in small steps of $\Delta\varepsilon = 0.01$. After each step, the structures underwent full relaxation, and the tension force ($\sigma = -\partial E_s/\partial l$) was determined from the strain energy. The corresponding behaviors of strain energy E_s, tension force σ, and atomic structures of strained $X_4OTe_9I_4$ ($X =$ Nb, Ti) nanowires are displayed in Fig. 3.

As shown in Figs. 3(a) and 3(b), the $Nb_4OTe_9I_4$ nanowire experiences three distinct stages under strains: (I) elastic deformation ($\varepsilon = 0$–0.11), (II) force-release stage ($\varepsilon = 0.12$–0.17), and (III) breaking stage ($\varepsilon = 0.18$–∞). However, the $Ti_4OTe_9I_4$ nanowire does not undergo the force-release stage before reaching the breaking point. Under the influence of axial-direction strain, it transitions directly from the elastic deformation stage (I: $\varepsilon = 0$–0.14) to the breaking stage (III: $\varepsilon = 0.15$–∞). In Stage I, a similar enhancement in strain energy E_s and a linear relationship (harmonic regime) between
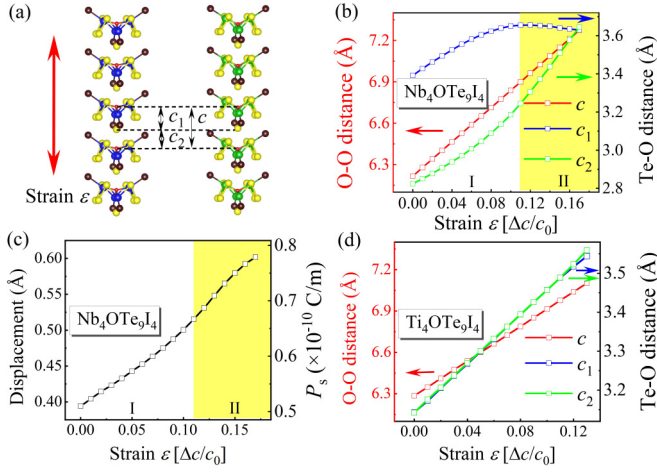
FIG. 4. (a) The schematic diagrams of $Nb_4OTe_9I_4$ and $Ti_4OTe_9I_4$ nanowire supercells. c is the lattice parameter. c_1 and c_2 represent the two Te-O distances between central Te atom and adjacent O atoms. The red arrow represents the direction of strain application. The values of c, c_1, and c_2 as a function of the tensile strain ε in the (b) $Nb_4OTe_9I_4$ and (d) $Ti_4OTe_9I_4$ nanowires. (c) The spontaneous polarization and displacement of central atoms as a function of the tensile strain ε in ferroelectric $Nb_4OTe_9I_4$ nanowire.

tension force σ and strain ε are evident in both $Nb_4OTe_9I_4$ and $Ti_4OTe_9I_4$ nanowires under a small tensile load. In particular, these two chain structures undergo a predominantly uniform expansion under axial strain, as shown in Figs. 3(c) and 3(d). In Stage II, distinct force behaviors are observed in the two nanostructures. For the $Nb_4OTe_9I_4$ nanowire, as the strain is further increased (exceeding 0.11), the force begins to exhibit a nonlinear behavior, indicative of a force release phenomenon. This implies a reduced force requirement to achieve additional elongation beyond the critical strain or maximum critical force. Despite the variation in force behavior, the atomic structure of the $Nb_4OTe_9I_4$ nanowire is maintained within the reversible elastic range at the end of Stage II, allowing the deformed nanowire to be optimized back to its initial structure. However, the $Ti_4OTe_9I_4$ nanowire does not undergo this force-release stage before breaking. This discrepancy can be attributed to the polarity-related structural differences between the two nanowires. During Stage III, the strain energy E_s for both nanowires deviates from the quadratic dependence as the tension increases further, and the structures fracture into two segments, bypassing the plastic deformation zone and directly entering the rupture zone. Thus, $Nb_4OTe_9I_4$ and $Ti_4OTe_9I_4$ nanowires exhibit elastic stretching capabilities up to $\varepsilon = 0.17$ and 0.14, respectively, indicating favorable mechanical features along the z axis. Notably, this behavior in the absence of a plastic deformation zone under the influence of strain differs from the reported characteristics of previously studied 1D chain materials, such as X_4SiTe_4 (X = Ta and Nb) and $Ta_2X_3Se_8$ (X = Pd and Pt) [20,21,65].

To further elucidate the force behavior in $X_4OTe_9I_4$ (X = Nb, Ti) nanowires, we subjected the two nanowires to strain along the z axis and recorded relevant structural data. As shown in Fig. 4, the structures of the two materials exhibit distinct trends under tension strain. Here, to gain a clearer

understanding of these different trends, we divide the lattice constant c of each nanowire into two parts, long side c_1 and short side c_2, which respectively represent the distances between the Te atom at the axis center and the two O atoms on each side [Fig. 4(a)]. For the $Nb_4OTe_9I_4$ nanowire, the chain structure is characterized by the relationship $c_1 > c_2$ due to the off-center displacement of the O ions. As shown in Fig. 4(b), as the nanowire is uniformly strained up to $\varepsilon \leqslant 0.11$ in Stage I, both c_1 and c_2 increase gradually. However, the growth rate of c_1 is slower than that of c_2. For $\varepsilon > 0.11$ in Stage II, c_1 exhibits negative growth, whereas c_2 continues to increase at a faster rate. Generally, c_1 and c_2 follow rules where the quadratic coefficients of quadratic functions are less and greater than zero, respectively. Therefore, the force release phenomenon in Stage II is primarily attributed to the distinct variations of c_1 and c_2 under tensile strain. Simultaneously, the difference in the variations of c_1 and c_2 is induced by the polar structure of the $Nb_4OTe_9I_4$ nanowire. The polarization-regulated mechanical properties play a crucial role in the applications of 1D $Nb_4OTe_9I_4$ materials in certain specialized ferroelectric fields. The strain-related polarization in Stages I and II before fracture is shown in Fig. 4(c). Before fracture, the polarization always increases with strain. However, due to the increased displacement of Te atoms in the force-release stage, the polarization growth rate in Stage II is significantly larger than that in Stage I. Ferroelectric materials often boast intricate crystalline structures, intricately arranged with multiple chemical elements. When subjected to tensile strain, the behavior of the Te atoms along the central axis, converging and contracting towards the cluster, suggests a reorganization of the electric dipole, serving as a mechanism to stabilize the polar structure. This process results in the partial alleviation of internal stress, demonstrated as the release of tensile force.

The anomalous force-release process has also been proposed in 1D Nb_4SiTe_4 nanowires [21]; however, the corresponding strain stage is small ($\varepsilon = 0.07–0.08$). The previously reported Nb_4SiTe_4 nanowire possesses a nonpolar chain structure that is different from that of the $Nb_4OTe_9I_4$ nanowire. The force-release phenomenon in the Nb_4SiTe_4 nanowires is attributed to the differential contraction rates of the inner and outer atomic tubes under tensile strain. This mechanism differs from that observed for the $Nb_4OTe_9I_4$ nanowire in this study. In addition, as shown in Fig. 4(a), the chain structure of the $Ti_4OTe_9I_4$ nanowire is characterized by the relationship $c_1 = c_2$. This relation can be maintained in the whole elastic stage, as shown by the well-established linear relationship between c_1 and c_2 with tensile strain in Fig. 4(d). This is also why we did not observe a force-release phenomenon in 1D $Ti_4OTe_9I_4$ system.

D. Electronic properties and doping-induced magnetism

In this section, we discuss the electronic structures of $X_4OTe_9I_4$ (X = Nb, Ti) nanowires. The electronic structures calculated using the HSE06 functional without the spin-orbital coupling (SOC) effect are shown in Figs. 5(a) and 5(b). In the case of the $Nb_4OTe_9I_4$ nanowire, the ferroelectric structure exhibits a near-direct band gap of 1.32 eV, where the conduction-band minimum (CBM) is located at Γ point and
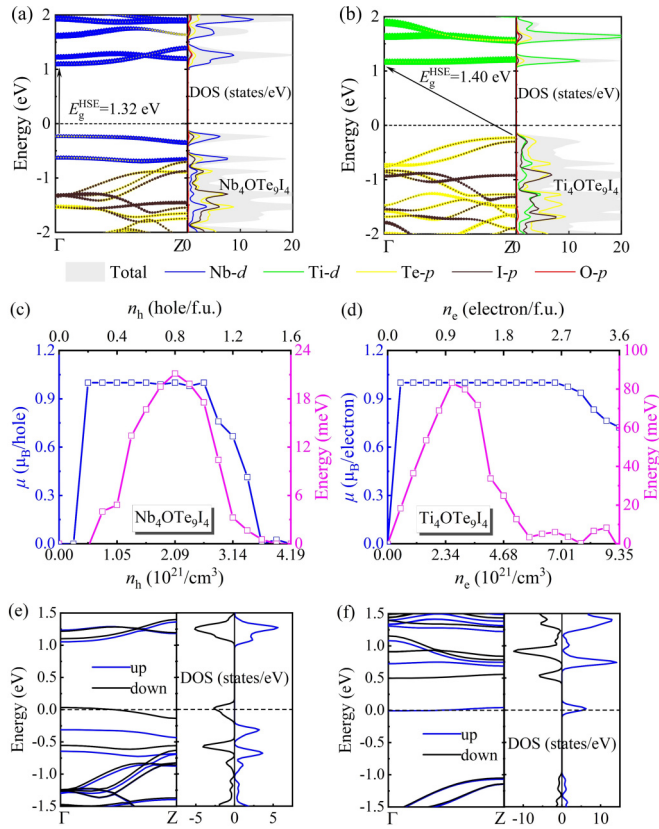
FIG. 5. The band structures and the projected density of states of (a) $Nb_4OTe_9I_4$ and (b) $Ti_4OTe_9I_4$ nanowires calculated by the HSE06 functionals. The Fermi level is set to zero with a black dashed line. The magnetic moments and spin-polarization energies as a function of the hole- and electron-doping concentration in the (c) $Nb_4OTe_9I_4$ and (d) $Ti_4OTe_9I_4$ nanowires. Spin-polarized band structures and density of states in the doping concentration of 0.4 hole and electron per formula unit for (e) $Nb_4OTe_9I_4$ and (f) $Ti_4OTe_9I_4$ nanowires.

the valence-band maximum (VBM) is also situated near the Γ point. The $Ti_4OTe_9I_4$ nanowire exhibits an indirect band gap of 1.40 eV, wherein the CBM is nearly at the Γ point and the VBM is located at the Z point. In addition to the different gap values for the two nanowires, the band structure dispersions are highly sensitive to the primary element. From the projected density of states (PDOS) shown in Figs. 5(a) and 5(b), we observe that both the CBM and VBM of the $Nb_4OTe_9I_4$ nanowire are predominantly contributed by the Nb-d states. However, the Ti-d and Te-p orbitals dominate the CBM and VBM in the $Ti_4OTe_9I_4$ nanowire, respectively. Thus, the difference between the direct and indirect band gaps of the $Nb_4OTe_9I_4$ and $Ti_4OTe_9I_4$ nanowires, respectively, is primarily due to variations in the orbital compositions of the VBM and CBM. Prominent peaks in the density of states (DOS) are visible in the VBM of the $Nb_4OTe_9I_4$ nanowire and the CBM of the $Ti_4OTe_9I_4$ nanowire. These phenomena are attributed to flat bands in the band structures. Generally, flat bands near the Fermi level can induce electronic instability, potentially inducing itinerant magnetism by doping carriers in nonmagnetic systems.

To investigate the potential for itinerant magnetism in $X_4OTe_9I_4$ (X = Nb, Ti) nanowires, we introduced either holes

or electrons into the valence or conduction band. As shown in Figs. 5(c) and 5(d), the magnetic moment suddenly rises to approximately $1\mu_B$ per hole (electron) at lower doping concentrations such as 0.2 hole per formula unit (hole/f.u.) for $Nb_4OTe_9I_4$ and 0.2 electron per formula unit (electron/f.u.) for $Ti_4OTe_9I_4$ nanowire. When the effective volumes of the nanowires are considered in the calculations, both hole and electron doping concentrations can be can be converted into three-dimensional units, equivalent to $0.52 \times 10^{21}/cm^3$. This doping concentration is small, making doping-induced magnetism more easily attainable in experimental settings for these two nanowires. Furthermore, the saturated magnetic moment of $1.0\mu_B$ per hole or electron can be sustained across a wide range of doping concentrations, such as 1.0 hole/f.u. and 2.6 electron/f.u. for $Nb_4OTe_9I_4$ and $Ti_4OTe_9I_4$ nanowires, respectively. The spin-polarization energies (defined as the energy difference between the nonmagnetic and magnetic states; $\Delta E = E_{NM} - E_M$) further validate the range of doping concentrations for the emergence of magnetism. The spin-polarization energies reach their maximum values when the doping concentrations are 0.8 hole/f.u. ($2.09 \times 10^{21}/cm^3$) and 1.0 electron/f.u. ($2.60 \times 10^{21}/cm^3$) for $Nb_4OTe_9I_4$ and $Ti_4OTe_9I_4$ nanowires, respectively. Positive values persist over a significant range of hole and electron concentrations, indicating that the magnetic ground state is more stable than the nonmagnetic state in these two nanowires.

Doping-induced magnetism can be explained using the Stoner model, in which itinerant magnetism occurs when the Stoner criterion $D(E_f)I > 1$ is satisfied [66]. Here, the Stoner parameter I represents the strength of the exchange interaction and is defined as $I = \Delta_{xc}/M$, with Δ_{xc} and M representing the exchange splitting energy of two spin channels near Fermi level and the spin magnetic moment of the unit cell, respectively. $D(E_f)$ is the non-spin-polarized DOS at the Fermi level. For example, when the doping concentrations are $n = 0.8$ hole/f.u. and 1.0 electron/f.u. for $Na_4OTe_9I_4$ and $Ti_4OTe_9I_4$ nanowires, respectively, the Stoner factors I are 0.93 and 1.30, and the $D(E_f)$ values are 12.87 and 17.34, respectively. These values satisfy the Stoner criterion, indicating that it is reasonable for the itinerant magnetism to emerge in both hole-doped $Nb_4OTe_9I_4$ and electron-doped $Ti_4OTe_9I_4$ nanowires.

Figure 5(e) shows the spin-polarized band structure of the $Nb_4OTe_9I_4$ nanowire at the doping concentration $n = 0.4$ hole/f.u. The breaking of spin degeneracy has a significant exchange splitting of approximately 0.35 eV. The spin-up band is fully occupied, whereas the spin-down band intersects the Fermi level. Thus, all the holes are introduced into the spin-down band, resulting in partial filling. For the $Ti_4OTe_9I_4$ nanowire, as shown in Fig. 5(f), the spin-polarized band structure at the doping concentration $n = 0.4$ electron/f.u. indicates greater spin splitting in the electron-doping $Ti_4OTe_9I_4$ nanowire (0.52 eV). In this scenario, the spin-up band crosses the Fermi level, whereas the spin-down band remains unoccupied. Thus, all the doping electrons are introduced into the spin-up bands. Consequently, hole and electron doping can transform the $Nb_4OTe_9I_4$ and $Ti_4OTe_9I_4$ nanowires into 1D half metals, highlighting their potential as ideal candidates for constructing spintronic devices. Although 1D magnetism is fascinating, its experimental observation at finite tempera-
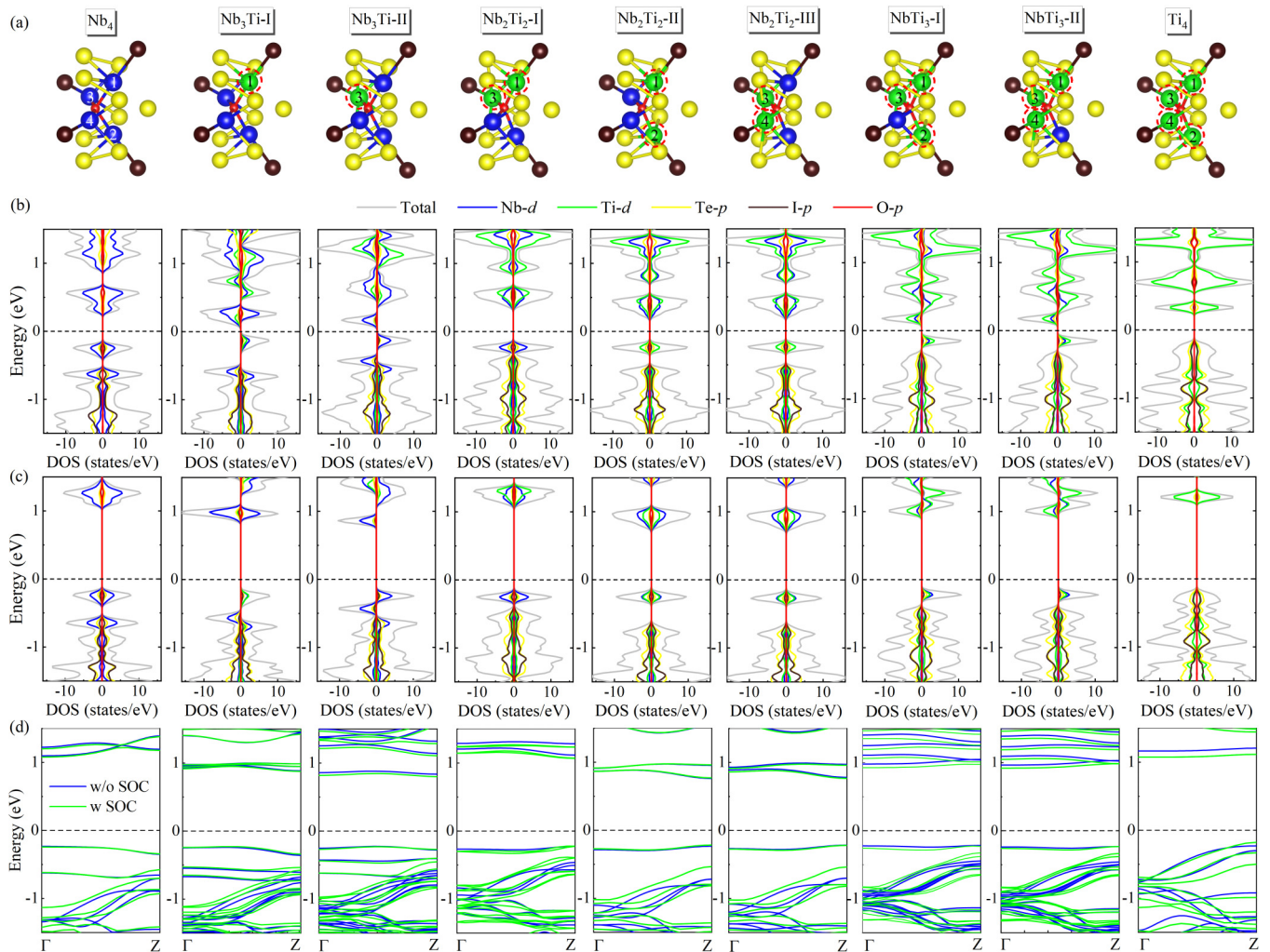
FIG. 6. (a) The structure diagrams of the pristine and alloying structures of the $Nb_4OTe_9I_4$ and $Ti_4OTe_9I_4$ nanowires. The corresponding projected density of states of these pristine and alloying structures calculated by the (b) PBE and (c) HSE06 functionals, respectively. (d) The corresponding band structures of these pristine and alloying structures calculated by the HSE06 functional with and without the SOC effect. The Fermi level is set to zero.

tures remains challenging. Fortunately, some 1D and quasi-1D magnetic materials including $CrSbSe_3$ [19], $CrZr_4Te_{14}$ [67], and $CrCl_3$ [68] have been successfully synthesized in experiment and their magnetic behaviors have been observed.

E. Alloying of metal elements

Achieving high doping concentrations can be challenging experimentally. In addition, magnetism can be induced by introducing electrons or holes through elemental substitution. Considering the variance in the outermost electrons, the principal elements of the $Nb_4OTe_9I_4$ and $Ti_4OTe_9I_4$ nanowires are Nb and Ti, which exhibit Nb^{5+} and Ti^{4+} behavior, respectively. This implies that the Ti atom loses one less electron than the Nb atom during bonding. Substituting one Nb atom with one Ti atom is akin to introducing a hole into the system. We hypothesize that this substitution may trigger magnetism akin to the theoretical doping of holes. Considering the structural similarity between $Nb_4OTe_9I_4$ and $Ti_4OTe_9I_4$ nanowires, alloying metallic elements (Nb and Ti) in the nanowire is relatively straightforward to achieve experimentally. Therefore,

we obtained alloy compounds with varying proportions of different metallic elements via elemental substitution, to investigate their electronic properties and potential magnetism. The potential alloy structures are shown in Fig. 6(a). For simplicity, $Nb_4OTe_9I_4$ and $Ti_4OTe_9I_4$ are abbreviated as Nb_4 and Ti_4, respectively. The alloy structures with different compositions are represented as Nb_3Ti, Nb_2Ti_2, and $NbTi_3$. According to structural symmetry, the four metal atoms (Nb or Ti) in a single unit cell are pairwise equivalent. As shown in Fig. 6(a), the Nb_3Ti system has two distinct structures: Nb_3Ti-I and Nb_3Ti-II; the Nb_2Ti_2 system has three structures: Nb_2Ti_2-I, Nb_2Ti_2-II, and Nb_2Ti_2-III; and $NbTi_3$ system has two structures: $NbTi_3$-I and $NbTi_3$-II.

We then track the optimized structures, PDOS, band gaps, and magnetic moments, as summarized in Fig. 6 and Table II. Here, the SOC correction is examined using the HSE06 functional for the pristine and alloying structures of the $Nb_4OTe_9I_4$ and $Ti_4OTe_9I_4$ nanowires, as shown in Fig. 6(d). The corresponding results of the two perfect structures, Nb_4 ($Nb_4OTe_9I_4$) and Ti_4 ($Ti_4OTe_9I_4$), are also shown for comparison. The effect of SOC on the band structures

TABLE II. The band gap, magnetic moment, and magnetic anisotropy energy (MAE) of pristine and alloying structures, Nb_4 ($Nb_4OTe_9I_4$), Nb_3Ti-I, Nb_3Ti-II, Nb_2Ti_2-I, Nb_2Ti_2-II, Nb_2Ti_2-III, $NbTi_3$-I, $NbTi_3$-II, and Ti_4 ($Ti_4OTe_9I_4$).

| System | Band gap (eV) | | | μ (μ_B) | MAE (μeV) |
	PBE	HSE06	HSE06+SOC		
Nb_4 ($Nb_4OTe_9I_4$)	0.54	1.32	1.32	0	
Nb_3Ti-I	0.24	1.12	1.11	1	139.5
Nb_3Ti-II	0.23	1.06	1.04	1	10.5
Nb_2Ti_2-I	0.61	1.35	1.29	0	
Nb_2Ti_2-II	0.45	1.00	0.98	0	
Nb_2Ti_2-III	0.45	1.00	0.98	0	
$NbTi_3$-I	0.31	1.20	1.15	1	51.5
$NbTi_3$-II	0.31	1.20	1.15	1	55.5
Ti_4 ($Ti_4OTe_9I_4$)	0.53	1.40	1.25	0	

is negligible. For example, the greatest change induced by the SOC effect in the band gap of the $Ti_4OTe_9I_4$ nanowire amounts to only 0.15 eV. For the Nb_3Ti-I and Nb_3Ti-II structures, the substitution of a Nb atom with a Ti atom can induce a magnetic moment of $1\mu_B$, which is akin to the effect of doping one fully spin-polarized hole. From the PDOS shown in Figs. 6(b) and 6(c), a substantial spin splitting near the Fermi level is observed, with magnetism predominantly originating from the d orbitals of Nb and Ti atoms. The spin-polarized charge density shown in Fig. 7 further confirms that the magnetic moments are mainly distributed in the Nb and Ti atoms and are partly derived from O atoms. Compared with the perfect $Nb_4OTe_9I_4$ structure, the one remaining unpaired electron introduced by the substitution of Ti atoms mainly occupies the spin-up orbital, whereas the spin-down orbital is unoccupied. Therefore, the Nb_3Ti-I and Nb_3Ti-II structures exhibit magnetic semiconductor characteristics with large band gaps of 1.11 (0.24) and 1.04 (0.23) eV at the HSE06 + SOC (PBE) level, respectively. For the Nb_2Ti_2 systems, the substitution of two Nb atoms with Ti atoms implies that the systems continue to introduce another hole, and thus the Fermi level
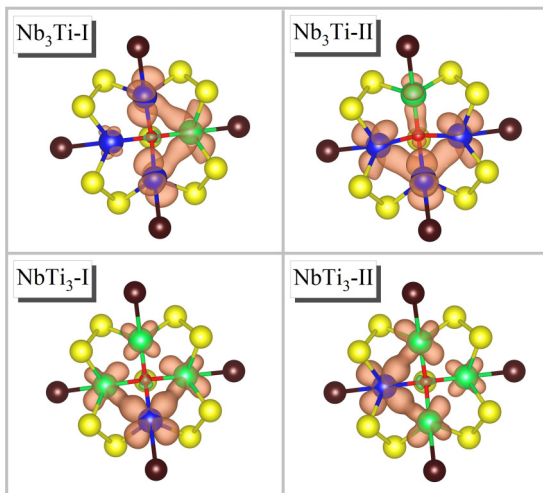

FIG. 7. The spin-polarized charge density of four magnetic configurations, Nb_3Ti-I, Nb_3Ti-II, $NbTi_3$-I, and $NbTi_3$-II. The spin-up and spin-down densities are labeled in brown and green, respectively.

continues to move down. In this case, the three alloying configurations (Nb_2Ti_2-I, Nb_2Ti_2-II, and Nb_2Ti_2-III) recover nonmagnetic semiconductor characteristics because the numbers of spin-down and spin-up electrons become equal. The Nb_2Ti_2-I configuration has a relatively large band gap of 1.29 (0.61) eV at the HSE06 + SOC (PBE) level, whereas the band gaps of Nb_2Ti_2-II and Nb_2Ti_2-III configurations are close and relatively small, approximately 0.98 (0.45) eV obtained using HSE06 + SOC (PBE) method. Notably, after structural optimization, the structures of Nb_2Ti_2-II and Nb_2Ti_2-III tend to converge. Therefore, Nb_2Ti_2-II and Nb_2Ti_2-III exhibit similar PDOS and band-gap values, as shown in Fig. 6. Finally, for the $NbTi_3$ systems, with the further reduction of electron number in the nanowire, a magnetic semiconductor system with a magnetic moment of $1\mu_B$ emerges again. Based on a thorough structural optimization, the structures of $NbTi_3$-I and $NbTi_3$-II are also highly similar, including bond lengths and bond angles. The band gaps of $NbTi_3$-I and $NbTi_3$-II are approximately 1.15 (0.31) eV at the HSE06 + SOC (PBE) level. From the PDOS shown in Figs. 6(b) and 6(c), a larger spin splitting appears near the Fermi level and the orbital occupied by the single electron has a spin-up configuration. The spin-polarized charge densities shown in Fig. 7 indicate that the magnetism mainly originates from the d orbitals of the Nb and Ti atoms.

The magnetocrystalline anisotropy (MCA) plays a fundamental role in inducing long-range magnetic ordering in low-dimensional materials. The MCA can be modulated using magnetic anisotropy energy (MAE). MAE is defined as the energy difference between the directions perpendicular to the chain (100 and 010) and parallel to the chain (001); $MAE = E_\perp - E_\parallel$. As listed in Table II, the MAE generated by the SOC effect for the four magnetic systems (Nb_3Ti-I, Nb_3Ti-II, $NbTi_3$-I, and $NbTi_3$-II) are 139.5, 10.5, 51.5, and 55.5 μeV, respectively. These positive values indicate that the easy magnetization axis of the 1D magnetic nanowires is aligned with the chain direction.

Alloying is an effective method for regulating the electronic and magnetic properties of low-dimensional materials. Several promising magnetic semiconductors have been obtained by alloying Nb and Ti in 1D $X_4OTe_9I_4$ nanowires. The band gaps of these systems could be regulated over a wide range, indicating that these nanowire materials may have potential applications in spintronic devices. With continuous improvements in experimental preparation techniques, nanowires with varying compositions of different metals can be synthesized.

F. Carrier mobility and conductivity

The carrier mobility is also a key parameter that determines the efficiency and performance of electronic and optoelectronic devices. The electrical properties can also be evaluated from carrier mobility. We examined the carrier mobilities of the $Nb_4OTe_9I_4$ and $Ti_4OTe_9I_4$ nanowires. According to the deformation potential (DP) theory [69], the carrier mobility of 1D systems is expressed as follows [70–74]:

$$\mu = \frac{e\hbar^2 C_{1D}}{(2\pi k_B T)^{\frac{1}{2}} |m^*|^{\frac{3}{2}} (E_1)^2},$$

TABLE III. 1D elastic constant C_{1D}, DP constant E_1, effective mass $|m^*|$, carrier mobility μ, and relaxation time τ for $Nb_4OTe_9I_4$ and $Ti_4OTe_9I_4$ nanowires along the chain direction at $T = 300$ K. h and e represent the holes and electrons, respectively.

System	C_{1D} ($\times 10^{-9}$ N)	E_1 (eV)		$|m^*|$ (m_0)		μ (cm^2 V^{-1} s^{-1})		τ (fs)	
		h	e	h	e	h	e	h	e
$Nb_4OTe_9I_4$	28.29	0.65	4.44	13.52	4.38	6.67	0.77	51.25	1.93
$Ti_4OTe_9I_4$	25.11	0.63	0.85	2.24	9.45	92.66	5.48	118.14	31.00

where e, $\hbar$, k_B, and T are the electron charge, reduced Planck constant, Boltzmann constant, and temperature, respectively. C_{1D} is the 1D chain elastic stiffness constant, given by $C_{1D} = (1/c_0)(\partial^2 E/\partial \varepsilon^2)$. E_1 is defined as $E_1 = |dE_{edge}/d\varepsilon|$, representing the displacements of the CBM for electrons and VBM for holes through altering the lattice, where E_{edge} is the energy of the conduction (or valence) band edge. The effective mass m^* can be calculated by $m^* = \pm\hbar^2(\partial^2 E/\partial k^2)^{-1}$, where $\partial^2 E/\partial k^2$ represents the second derivative of the energy dispersion with respect to the wave vector k. The corresponding values of C_{1D}, E_1, $|m^*|$, and carrier mobility μ for 1D $Nb_4OTe_9I_4$ and $Ti_4OTe_9I_4$ nanowires are all summarized in Table III.

The $Nb_4OTe_9I_4$ nanowire possesses relatively large effective masses, m^*, $13.52m_0$ and $4.38m_0$, for holes and electrons, respectively. As shown in Fig. 5(a), this is primarily due to the relatively flat-band edges (d orbitals of Nb atoms) near the CBM and VBM of the $Nb_4OTe_9I_4$ nanowire. Besides, the DP constant for electrons is 4.44 eV, which is higher than that for holes (0.65 eV). These lead to small hole and electron mobilities, 6.67 and 0.77 cm^2 V^{-1} s^{-1}, respectively, in the $Nb_4OTe_9I_4$ nanowire. As shown in Fig. 5(b), with the substitution of the metal element from Nb to Ti, the relatively flat band contributed by the d orbitals of Ti atoms are only located near the CBM, while the band near the VBM that is contributed by the p orbitals of Te atoms is relatively dispersive, causing a large effective mass of $9.45m_0$ for electrons and relatively small effective mass of $2.24m_0$ for holes. Simultaneously, small DP constants for both holes (0.63 eV) and electrons (0.85) are obtained in the $Ti_4OTe_9I_4$ nanowire. This situation increases the hole and electron mobility rapidly to 92.66 and 5.48 cm^2 V^{-1} s^{-1}, respectively. This high hole mobility is

larger than those of previously reported 1D chain materials, such as Sn_2X_3 ($X = S$, Se) [75], indicating the potential device applications of such nanowire materials.

The average scattering relaxation time can be expressed as $\tau = |m^*|\mu/e$. As summarized in Table III, although the relaxation time is determined by both the effective mass and carrier mobility, the hole mobilities of $Nb_4OTe_9I_4$ and $Ti_4OTe_9I_4$ nanowires are significantly higher than their electron mobilities, which directly leads to a higher relaxation time for holes compared with those for electrons. Based on the Boltzmann transport theory, we performed the calculations on the conductivities of $Nb_4OTe_9I_4$ and $Ti_4OTe_9I_4$ nanowires, with conductivity described as $\sigma = ne\mu$, where n is carrier concentration. As shown in Fig. 8, the conductivities increase linearly with the enhancement in optimal carrier concentration. Moreover, the hole mobilities of $Nb_4OTe_9I_4$ and $Ti_4OTe_9I_4$ significantly surpass the electron mobilities. As a consequence, hole conductivities are one to two orders of magnitude greater than electron conductivities, showcasing typical attributes of p-type materials. This aspect holds considerable promise for applications in the realm of thermoelectricity.

IV. CONCLUSIONS

We conducted a detailed investigation of the structural, ferroelectric, electronic, mechanical, and magnetic properties of 1D $X_4OTe_9I_4$ ($X = $ Nb, Ti) nanowires using first-principles calculations. The different electron counts of the Nb and Ti metal atoms result in distinct chemical bonding coordination environments for the $Nb_4OTe_9I_4$ and $Ti_4OTe_9I_4$ nanowires, leading to differences in their structures and physical properties. Our calculations revealed that intrinsic ferroelectric polarization ordering existed only in the $Nb_4OTe_9I_4$ nanowire, which was attributed to the off-center displacement of O atoms relative to the center of Nb_4 clusters. The spontaneous polarization of the $Nb_4OTe_9I_4$ nanowire was also enhanced by applying a tensile strain. However, the $Ti_4OTe_9I_4$ nanowire was a nonferroelectric material because the bonds between the four Ti and O atoms were almost identical. For the ferroelectric $Nb_4OTe_9I_4$ nanowire under strain conditions, the stored strain energy could drive different rates of change in the distances between the Te atom and two adjacent O atoms at the axis center, which led to an unexpected force-releasing stage to stabilize the polar configuration. However, the corresponding Te-O distances in the nonferroelectric $Ti_4OTe_9I_4$ nanowire uniformly increases with tensile strain. From the results of HSE06 + SOC calculations, the $Nb_4OTe_9I_4$ and $Ti_4OTe_9I_4$ nanowires were direct- and indirect-band-gap semiconductors with moderate gaps of 1.32 and 1.25 eV, respectively. Itinerant magnetism was introduced into the flat bands near the
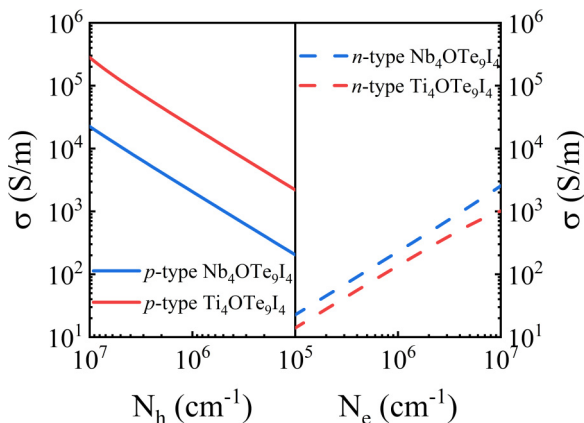

FIG. 8. The conductivity as a function of carrier concentration in the $Nb_4OTe_9I_4$ and $Ti_4OTe_9I_4$ nanowires.

Fermi level in the two nanowires by doping with holes or electrons. The saturated magnetic moment was maintained at $1.0\mu_B$ for a wide range of doping concentrations. Considering the structural resemblance between $Nb_4OTe_9I_4$ and $Ti_4OTe_9I_4$ nanowires, the alloying of metal elements (Nb and Ti) within the nanowires was relatively straightforward to accomplish experimentally. Our calculations demonstrated that 1D alloys with different proportions of $Nb_4OTe_9I_4$ and $Ti_4OTe_9I_4$ nanowires might exhibit magnetic-semiconductor characteristics with large band gaps. These results indicate that the $Nb_4OTe_9I_4$ nanowire provide a solid platform for studying the multifunctional properties of 1D materials, with the corresponding results awaiting experimental confirmation.

[1] K. S. Novoselov, A. K. Geim, S. V. Morozov, D. Jiang, Y. Zhang, S. V. Dubonos, I. V. Grigorieva, and A. A. Firsov, Electric field effect in atomically thin carbon films, Science **306**, 666 (2004).

[2] D. Teweldebrhan, V. Goyal, and A. A. Balandin, Exfoliation and characterization of bismuth telluride atomic quintuples and quasi-two-dimensional crystals, Nano Lett. **10**, 1209 (2010).

[3] A. B. Alexander, Thermal properties of graphene and nanostructured carbon materials, Nat. Mater. **10**, 569 (2011).

[4] J. Zhang, C. Fu, S. Song, H. Du, D. Zhao, H. Huang, L. Zhang, J. Guan, Y. Zhang, X. Zhao, C. Ma, C. Jia, and D. Tománek, Changing the phosphorus allotrope from a square columnar structure to a planar zigzag nanoribbon by increasing the diameter of carbon nanotube nanoreactors, Nano Lett. **20**, 1280 (2020).

[5] S. N. Shirodkar and U. V. Waghmare, Emergence of ferroelectricity at a metal-semiconductor transition in a $1T$ monolayer of MoS_2, Phys. Rev. Lett. **112**, 157601 (2014).

[6] Q. H. Wang, K. Kalantar-Zadeh, A. Kis, J. N. Coleman, and M. S. Strano, Electronics and optoelectronics of two-dimensional transition metal dichalcogenides, Nat. Nanotechnol. **7**, 699 (2012).

[7] W. Gao, X. Shi, Y. Qiao, M. Yu, and H. Yin, Strain-dependent near-zero and negative Poisson ratios in a two-dimensional $(CuI)P_4Se_4$ monolayer, Phys. Rev. B **109**, 075402 (2024).

[8] Y. Xia, P. Yang, Y. Sun, Y. Wu, B. Mayers, B. Gates, Y. Yin, F. Kim, and H. Yan, One-dimensional nanostructures: Synthesis, characterization, and applications, Adv. Mater. **15**, 353 (2003).

[9] L. Cademartiri and G. A. Ozin, Ultrathin nanowires—A materials chemistry perspective, Adv. Mater. **21**, 1013 (2009).

[10] T. Li, Y. Liu, S. Porter, and J. E. Goldberger, Dimensionally reduced one-dimensional chains of $TiSe_2$, Chem. Mater. **25**, 1477 (2013).

[11] X. Duan and C. M. Lieber, General synthesis of compound semiconductor nanowires, Adv. Mater. **12**, 298 (2000).

[12] N. P. Dasgupta, J. Sun, C. Liu, S. Brittman, S. C. Andrews, J. Lim, H. Gao, R. Yan, and P. Yang, 25th anniversary article: Semiconductor nanowires-synthesis, characterization, and applications, Adv. Mater. **26**, 2137 (2014).

[13] G. Cao and D. Liu, Template-based synthesis of nanorod, nanowire, and nanotube arrays, Adv. Colloid Interface Sci. **136**, 45 (2008).

[14] D. J. Sellmyer, M. Zheng, and R. Skomski, Magnetism of Fe, Co and Ni nanowires in self-assembled arrays, J. Phys.: Condens. Matter **13**, R433 (2001).

[15] M. Nagata, S. Shukla, Y. Nakanishi, Z. Liu, Y. Lin, T. Shiga, Y. Nakamura, T. Koyama, H. Kishida, T. Inoue, N. Kanda, S. Ohno, Y. Sakagawa, K. Suenaga, and H. Shinohara, Isolation of single-wired transition-metal monochalcogenides by carbon nanotubes, Nano Lett. **19**, 4845 (2019).

[16] N. Kanda, Y. Nakanishi, D. Liu, Z. Liu, T. Inoue, Y. Miyata, D. Tománek, and H. Shinohara, Efficient growth and characterization of one-dimensional transition metal tellurides inside carbon nanotubes, Nanoscale **12**, 17185 (2020).

[17] E. Andharia, T. P. Kaloni, G. J. Salamo, S.-Q. Yu, H. O. H. Churchill, and S. Barraza-Lopez, Exfoliation energy, quasiparticle band structure, and excitonic properties of selenium and tellurium atomic chains, Phys. Rev. B **98**, 035420 (2018).

[18] S. Oh, S. Chae, B. J. Kim, A. J. Siddiqa, K. H. Choi, W. Jang, K. H. Lee, H. Y. Kim, D. K. Lee, Y. Kim, H. K. Yu, and J. Choi, Inorganic molecular chain Nb_2Se_9: Synthesis of bulk crystal and one-atom-thick level exfoliation, Phys. Status Solidi RRL **12**, 1800451 (2018).

[19] Y. Qu, M. Q. Arguilla, Q. Zhang, X. He, and M. Dincă, Ultrathin, high-aspect ratio, and free-standing magnetic nanowires by exfoliation of ferromagnetic quasi-one-dimensional van der Waals lattices, J. Am. Chem. Soc. **143**, 19551 (2021).

[20] S. Liu, H. Yin, D. J. Singh, and P. F. Liu, Ta_4SiTe_4: A possible one-dimensional topological insulator, Phys. Rev. B **105**, 195419 (2022).

[21] S. Liu, H. Yin, and P. F. Liu, Strain-dependent electronic and mechanical properties in one-dimensional topological insulator Nb_4SiTe_4, Phys. Rev. B **108**, 045411 (2023).

[22] F. Zhang, L. Kang, C. Liu, B. Wang, and H. Yin, The polarization-modulated electronic structure and giant tunneling-electroresistance effect of a one-dimensional ferroelectric $Ta_4OTe_9I_4$ nanowire, Appl. Phys. Lett. **123**, 202903 (2023).

[23] J. F. Scott, Applications of modern ferroelectrics, Science **315**, 954 (2007).

[24] J. F. Scott and C. A. Paz de Araujo, Ferroelectric memories, Science **246**, 1400 (1989).

[25] M. Y. Zhuravlev, R. F. Sabirianov, S. S. Jaswal, and E. Y. Tsymbal, Giant electroresistance in ferroelectric tunnel junctions, Phys. Rev. Lett. **94**, 246802 (2005).

[26] B. A. Hernandez, K. Chang, E. R. Fisher, and P. K. Dorhout, Sol-gel template synthesis and characterization of $BaTiO_3$ and $PbTiO_3$ nanotubes, Chem. Mater. **14**, 480 (2002).

[27] P. M. Rørvik, T. Grande, and M. Einarsrud, One-dimensional nanostructures of ferroelectric perovskites, Adv. Mater. **23**, 4007 (2011).

[28] C. Yang, M. Chen, S. Li, X. Zhang, C. Hua, H. Bai, C. Xiao, S. A. Yang, P. He, Z. Xu, and Y. Lu, Coexistence of ferroelectricity and ferromagnetism in one-dimensional SbN and BiN nanowires, ACS Appl. Mater. Interfaces **13**, 13517 (2021).

[29] L. Lin, Y. Zhang, A. Moreo, E. Dagotto, and S. Dong, Quasi-one-dimensional ferroelectricity and piezoelectricity in WOX_4 halogens, Phys. Rev. Mater. **3**, 111401(R) (2019).

[30] J. Zhang, J. Guan, S. Dong, and B. I. Yakobson, Room-temperature ferroelectricity in group-IV metal chalcogenide nanowires, J. Am. Chem. Soc. **141**, 15040 (2019).

[31] T. Chowdhury, C. Taneja, A. Vasdev, P. Ghosh, G. Sheet, G. V. P. Kumar, and A. Rahman, Stacking engineered room temperature ferroelectricity in twisted germanium sulfide nanowires, Adv. Electron. Mater. **8**, 2101158 (2022).

[32] A. Vasylenko, S. Marks, J. M. Wynn, P. V. C. Medeiros, Q. M. Ramasse, A. J. Morris, J. Sloan, and D. Quigley, Electronic structure control of sub-nanometer 1D SnTe *via* nanostructuring within single-walled carbon nanotubes, ACS Nano **12**, 6023 (2018).

[33] K. Chang, J. Liu, H. Lin, N. Wang, K. Zhao, A. Zhang, F. Jin, Y. Zhong, X. Hu, W. Duan, Q. Zhang, L. Fu, Q. Xue, X. Chen, and S. Ji, Discovery of robust in-plane ferroelectricity in atomic-thick SnTe, Science **353**, 274 (2016).

[34] Y. Zhao, Y. Guo, Y. Qi, X. Jiang, Y. Su, and J. Zhao, Coexistence of ferroelectricity and ferromagnetism in fullerene-based one-dimensional chains, Adv. Sci. (Weinheim, Ger.) **10**, 2301265 (2023).

[35] D. P. Huang, C. C. Huang, S. X. Liu, H. D. Xu, and J. L. Huang, An oxygen-centred tetranuclear tantalum cluster: $Ta_4O(Te_2)_4TeI_4$, Acta Crystallogr., Sect. C: Struct. Chem. **54**, 893 (1998).

[36] W. Tremel, $Nb_4OTe_9I_4$: A one-dimensional chain compound containing tetranuclear oxygen-centred niobium clusters, J. Chem. Soc., Chem. Commun. **9**, 709 (1992).

[37] L. Shi-Xiong, D. Huang, C. Huang, H. Xu, and J. Huang, A new extended tetranuclear titanium cluster: $Ti_4O(Te_2)_4TeI_4$, J. Solid State Chem. **123**, 273 (1996).

[38] S. Artemkina, R. Galiev, P. Poltarak, V. Komarov, Y. Gayfulin, A. Lavrov, and V. Fedorov, Vanadium O-centered selenoiodide complex: Synthesis and structure of $V_4O(Se_2)_4I_6 \cdot I_2$, Inorg. Chem. (Washington, DC, U. S.) **60**, 17627 (2021).

[39] P. Poltarak, V. Komarov, Y. Gayfulin, S. Artemkina, and V. Fedorov, New O-centered titanium chalcohalide: Synthesis and structure of $Ti_4O(Se_2)_4Br_6$, Z. Anorg. Allg. Chem. **647**, 1729 (2021).

[40] F. A. Cotton, X. Feng, P. A. Kibala, and R. B. W. Sandor, An oxygen-centered tetranuclear titanium compound $Ti_4O(S_2)_4Cl_6$, J. Am. Chem. Soc. **111**, 2148 (1989).

[41] M. N. Sokolov, A. L. Gushchin, P. A. Abramov, A. V. Virovets, E. V. Peresypkina, S. G. Kozlova, B. A. Kolesov, C. Vicent, and V. P. Fedin, Synthesis and structure of $Ta_4S_9Br_8$. An emergent family of early transition metal chalcogenide clusters, Inorg. Chem. (Washington, DC, U. S.) **44**, 8756 (2005).

[42] M. N. Sokolov, A. L. Gushchin, A. V. Virovets, E. V. Peresypkina, S. G. Kozlova, and V. P. Fedin, Synthesis and characterization of a novel tantalum chalcogen-rich molecular cluster with square planar metal core, Inorg. Chem. (Washington, DC, U. S.) **43**, 7966 (2004).

[43] Y. V. Mironov, S. S. Yarovoi, D. Y. Naumov, S. G. Kozlova, V. N. Ikorsky, R. K. Kremer, A. Simon, and V. E. Fedorov, $V_4S_9Br_4$: A novel high-spin vanadium cluster thiobromide with square-planar metal core, J. Phys. Chem. B **109**, 23804 (2005).

[44] V. K. Greenacre, W. Levason, G. Reid, and D. E. Smith, Coordination complexes and applications of transition metal sulfide and selenide halides, Coord. Chem. Rev. **424**, 213512 (2020).

[45] V. E. Fedorov, Y. V. Mironov, N. G. Naumov, M. N. Sokolov, and V. P. Fedin, Chalcogenide clusters of group 5–7 metals, Russ. Chem. Rev. **76**, 529 (2007).

[46] V. E. Fedorov, A. V. Mishchenko, and V. P. Fedin, Cluster transition metal chalcogenide halides, Russ. Chem. Rev. **54**, 408 (1985).

[47] R. P. Ziebarth and J. D. Corbett, Centered zirconium chloride clusters. synthetic and structural aspects of a broad solid-state chemistry, Acc. Chem. Res. **22**, 256 (1989).

[48] G. Kresse and J. Furthmüller, Efficiency of *ab-initio* total energy calculations for metals and semiconductors using a plane-wave basis set, Comput. Mater. Sci. **6**, 15 (1996).

[49] G. Kresse and J. Furthmüller, Efficient iterative schemes for *ab initio* total-energy calculations using a plane-wave basis set, Phys. Rev. B **54**, 11169 (1996).

[50] J. P. Perdew, K. Burke, and M. Ernzerhof, Generalized gradient approximation made simple, Phys. Rev. Lett. **77**, 3865 (1996).

[51] S. Grimme, J. Antony, S. Ehrlich, and H. Krieg, A consistent and accurate *ab initio* parametrization of density functional dispersion correction (DFT-D) for the 94 elements H–Pu, J. Chem. Phys. **132**, 154104 (2010).

[52] J. Heyd, G. E. Scuseria, and M. Ernzerhof, Hybrid functionals based on a screened Coulomb potential, J. Chem. Phys. **118**, 8207 (2003).

[53] G. Kresse, J. Furthmüller, and J. Hafner, *Ab initio* force constant approach to phonon dispersion relations of diamond and graphite, Europhys. Lett. **32**, 729 (1995).

[54] R. D. King-Smith and D. Vanderbilt, Theory of polarization of crystalline solids, Phys. Rev. B **47**, 1651 (1993).

[55] D. Vanderbilt, Berry-phase theory of proper piezoelectric response, J. Phys. Chem. Solids **61**, 147 (2000).

[56] D. Sheppard, P. Xiao, W. Chemelewski, D. D. Johnson, and G. Henkelman, A generalized solid-state nudged elastic band method, J. Chem. Phys. **136**, 074103 (2012).

[57] G. Henkelman, B. P. Uberuaga, and H. Jónsson, A climbing image nudged elastic band method for finding saddle points and minimum energy paths, J. Chem. Phys. **113**, 9901 (2000).

[58] G. K. H. Madsen, J. Carrete, and M. J. Verstraete, BoltzTraP2, a program for interpolating band structures and calculating semiclassical transport coefficients, Comput. Phys. Commun. **231**, 140 (2018).

[59] H. L. Zhuang and R. G. Hennig, Computational search for single-layer transition-metal dichalcogenide photocatalysts, J. Phys. Chem. C **117**, 20440 (2013).

[60] B. Tuttle, S. Alhassan, and S. Pantelides, Computational predictions for single chain chalcogenide-based one-dimensional materials, Nanomaterials **7**, 115 (2017).

[61] R. Resta, M. Posternak, and A. Baldereschi, Towards a quantum theory of polarization in ferroelectrics: The case of $KNbO_3$, Phys. Rev. Lett. **70**, 1010 (1993).

[62] R. E. Cohen, Origin of ferroelectricity in perovskite oxides, Nature (London) **358**, 136 (1992).

[63] A. Chandrasekaran, A. Mishra, and A. K. Singh, Ferroelectricity, antiferroelectricity, and ultrathin 2D electron/hole gas

in multifunctional monolayer MXene, Nano Lett. **17**, 3290 (2017).

[64] Z. Wang, N. Ding, C. Gui, S. S. Wang, M. An, and S. Dong, Ferroelectricity in strained Hf_2CF_2 monolayer, Phys. Rev. Mater. **5**, 074408 (2021).

[65] E. V. Sukhanova and P. B. Sorokin, Specific response of the atomic and electronic structure of $Ta_2Pd_3Se_8$ and $Ta_2Pt_3Se_8$ nanoribbons to the uniaxial strain, J. Phys. Chem. C **124**, 7539 (2020).

[66] E. C. Stoner, Collective electron ferromagnetism II. Energy and specific heat, Proc. R. Soc. London, Ser. A **169**, 339 (1939).

[67] Y. Fang, K. Yang, E. Zhang, S. Liu, Z. Jia, Y. Zhang, H. Wu, F. Xiu, and F. Huang, Quasi-1D van der Waals antiferromagnetic $CrZr_4Te_{14}$ with large in-plane anisotropic negative magnetoresistance, Adv. Mater. **34**, 2200145 (2022).

[68] Y. Li, A. Li, H. Li, J.and Tian, Z. Zhang, S. Zhu, R. Zhang, S. Liu, K. Cao, L. Kang, and Q. Li, Eficient synthesis of highly crystalline one-dimensional $CrCl_3$ atomic chains with a spin glass statef, ACS Nano **17**, 20112 (2023).

[69] J. Bardeen and W. Shockley, Deformation potentials and mobilities in non-polar crystals, Phys. Rev. **80**, 72 (1950).

[70] X. Zhang, X. Zhao, D. Wu, Y. Jing, and Z. Zhou, High and anisotropic carrier mobility in experimentally possible Ti_2CO_2 (MXene) monolayers and nanoribbons, Nanoscale **7**, 16020 (2015).

[71] G. Wang, Density functional study on the increment of carrier mobility in armchair graphene nanoribbons induced by Stone–Wales defects, Phys. Chem. Chem. Phys. **13**, 11939 (2011).

[72] M. Long, L. Tang, D. Wang, L. Wang, and Z. Shuai, Theoretical predictions of size-dependent carrier mobility and polarity in graphene, J. Am. Chem. Soc. **131**, 17728 (2009).

[73] B. Xu, Y. D. Xia, J. Yin, X. G. Wan, K. Jiang, A. D. Li, D. Wu, and Z. G. Liu, The effect of acoustic phonon scattering on the carrier mobility in the semiconducting zigzag single wall carbon nanotubes, Appl. Phys. Lett. **96**, 183108 (2010).

[74] F. B. Beleznay, F. Bogár, and J. Ladik, Charge carrier mobility in quasi-one-dimensional systems: Application to a guanine stack, J. Chem. Phys. **119**, 5690 (2003).

[75] R. Sen and P. Johari, One-dimensional-Sn_2X_3 (X = S, Se) as promising optoelectronic and thermoelectronic materials: A comparison with three-dimensional-Sn_2X_3, ACS Appl. Mater. Interfaces **11**, 12733 (2019).